



# Introducing highly polarizable cation in M-N-C type catalysts to boost their oxygen reduction reaction performance

Rui Sui<sup>a,1</sup>, Jing Chai<sup>b,1</sup>, Xuerui Liu<sup>a,1</sup>, Jiajing Pei<sup>a</sup>, Xuejiang Zhang<sup>a</sup>, Xingdong Wang<sup>a</sup>, Yu Wang<sup>d</sup>, Juncai Dong<sup>e</sup>, Wei Zhu<sup>a</sup>, Wenxing Chen<sup>c,\*</sup>, Liang Zhang<sup>b,\*</sup>, Zhongbin Zhuang<sup>a,\*</sup>

<sup>a</sup> State Key Lab of Organic-Inorganic Composites and Beijing Advanced Innovation Center for Soft Matter Science and Engineering, Beijing University of Chemical Technology, Beijing 100029, China

<sup>b</sup> School of Vehicle and Mobility, Tsinghua University, Beijing, China

<sup>c</sup> Energy & Catalysis Center, School of Materials Science and Engineering, Beijing Institute of Technology, Beijing 100081, China

<sup>d</sup> Shanghai Synchrotron Radiation Facility, Shanghai Institute of Applied Physics, Chinese Academy of Science, Shanghai 201800, China

<sup>e</sup> Beijing Synchrotron Radiation Facility, Institute of High Energy Physics, Chinese Academy of Sciences, Beijing 100049, China

## ARTICLE INFO

### Keywords:

Metal-nitrogen-carbon materials  
Oxygen reduction reaction  
Fuel cells  
Highly polarizable metal cation  
Electrochemistry

## ABSTRACT

The metal-nitrogen-carbon (M-N-C) type oxygen reduction reaction (ORR) catalysts are promising for hydroxide exchange membrane fuel cells, but catalysts with further improved performance are challenging. Here, we report the efficient improvement of the ORR activity of M-N-C catalysts by employing highly polarizable metal cation Ag<sup>+</sup>. Ag, Fe single atomic sites embedded in concave nitrogen doped carbon (Ag<sub>1</sub>Fe<sub>1</sub>/CNC) is successfully synthesized and shows high performance towards ORR, indicating by both the ultra-high half-wave potential of 0.917 V and membrane electrolyte assembly performance of peak power density up to 1.26 W cm<sup>-2</sup>. The binding energy of the ORR intermediates on the highly polarizable Ag site in Ag<sub>1</sub>Fe<sub>1</sub>/CNC was significantly tuned by the adjacent Fe site by more than 0.2 eV, and thus leading to a low theoretical ORR overpotential of only 0.398 V. The employment of the highly polarizable metal cation brings a novel and efficient approach to construct highly active catalysts.

## 1. Introduction

The fuel cells are the promising energy conversion devices that can produce electricity cleanly, efficiently, and sustainably [1–3]. However, the high cost of the fuel cells, in which the requirement of the precious-metal-based catalysts contributed to the major parts, hindered their wide applications [4–6]. The recently developed hydroxide exchange membrane fuel cells (HEMFCs) provide basic reaction condition, which brings the possibility to use precious-metal-free catalysts and cheaper bipolar plates, and thus may reduce the cost of the fuel cells [7–10]. The metal-nitrogen-carbon (M-N-C) type catalysts have shown promising oxygen reduction reaction (ORR) activity in alkaline condition, which could be served as the cathode for HEMFCs [11–15]. However, there are still more than 300 mV of overpotential required by using the state-of-the-art M-N-C catalysts [16–20]. And more important, the performance of the HEMFCs using the M-N-C as the cathode catalyst still have gaps to those using precious metal-based catalysts [21,22]. Highly

active M-N-C catalysts are still desired but challenging.

To improve the activities of the M-N-C catalysts, the properties of the catalytic active centers need to be adjusted [23,24]. The metal centers are generally considered as the active sites for the ORR in alkaline condition [25,26]. The O<sub>2</sub> adsorbed on the metal sites and then transferred electrons and reduced to hydroxides. The binding strength to the oxygen related intermediates are considered as the descriptor to the activity of the ORR catalysts [27–30]. Adjusting the electronic structures of the active sites, which tunes the binding energies to the intermediates, could improve the activities of the catalyst [31–35]. Regulating the coordinating environment of the metal centers was found a feasible approach. For example, the previous studies shown that by introducing hetero coordination atoms besides N, such as S and P, the ORR activities can be enhanced [36–39]. The electronic structure of the metal centers in the M-N-C catalyst is influenced by the adjacent catalytic active centers as well [40–43]. Thus, the dual metal site M-N-C catalysts, with the synergistic effect that the tuned by the adjacent hetero metal centers,

\* Corresponding authors.

E-mail addresses: [wxchen@bit.edu.cn](mailto:wxchen@bit.edu.cn) (W. Chen), [zhangbright@tsinghua.edu.cn](mailto:zhangbright@tsinghua.edu.cn) (L. Zhang), [zhuangzb@mail.buct.edu.cn](mailto:zhuangzb@mail.buct.edu.cn) (Z. Zhuang).

<sup>1</sup> R. Sui, J. Chai, and X. Liu contributed equally to this work.

have also proposed to improve the ORR activity.

To achieve a more efficient tuning, the active centers need to be easily adjusted. However, the tenability of the metal centers has seldom considered. To efficiently modify the electronic structure of the active sites, it requires the electronic clouds around the metal active centers are easily adjusted [44–47]. Polarizability is defined as the ease with which the electron cloud of an atom, ion or molecule is distorted, so it refers to the level of the change of the electron. Although compared with anions, cations are not highly polarizable, the electronic structure of cations are affected by the environments. Generally, the cations with large radius have higher polarizabilities, and their electronic clouds are easier to distort. The  $\text{Ag}^+$  has large radius of 1.00 Å, which is much larger than the commonly used cation in the M-N-C type catalysts, such as  $\text{Fe}^{2+}$  (0.63 Å),  $\text{Co}^{2+}$  (0.56 Å),  $\text{Ni}^{2+}$  (0.49 Å), and  $\text{Mn}^{2+}$  (0.66 Å) [48–50], leading to the high polarizability of  $\text{Ag}^+$ . Ag is also a promising platinum-group-metal free ORR catalyst for HEMFC [51–54]. Introducing the Ag into M-N-C type catalyst and further tuning its electronic structures may provide new opportunity in catalyst development.

Herein, we report the Ag, Fe single atomic sites embedded in concave nitrogen doped carbon ( $\text{Ag}_1\text{Fe}_1/\text{CNC}$ , the subscripted 1 denoted the single atomic sites), which shows high-performance towards for ORR in both rotating disk electrode (RDE) test and HEMFC. Beneficial from the highly polarizable Ag sites and the tuning effect from the adjunct Fe sites, which has higher valance state giving high polarizing power, the  $\text{Ag}_1\text{Fe}_1/\text{CNC}$  shows an ultra-high ORR half-wave potential ( $E_{1/2}$ ) of 0.917 V (vs. RHE, the same hereafter), which is better than that of commercial Pt/C and almost all of the reported M-N-C type ORR catalysts. The HEMFC employing the  $\text{Ag}_1\text{Fe}_1/\text{CNC}$  as the cathode catalyst delivers a high peak power density of  $1.26 \text{ W cm}^{-2}$ . The density function theory (DFT) calculation demonstrates the high ORR performance originated from the Ag sites, which has a low theoretical overpotential of 0.398 V. This low overpotential is achieved by the tuning effect from the adjunct Fe hetero-atoms, which make the Ag sites in  $\text{Ag}_1\text{Fe}_1/\text{CNC}$  has the theoretical overpotential reduced by more than 0.2 V compared with the pristine Ag–N<sub>3</sub> sites. And this large difference is attributed to the high polarizability of the Ag sites. This work demonstrates the advantages of the highly tunable metal sites through high polarizability in electrocatalysis, which gives a novel strategy in catalyst design.

## 2. Experimental section

### 2.1. Chemicals

Silver trifluoroacetate ( $\text{C}_2\text{AgF}_3\text{O}_2$ ), iron(III) nitrate nonahydrate ( $\text{Fe}(\text{NO}_3)_3 \cdot 9\text{H}_2\text{O}$ ), cetyltrimethylammonium bromide (CTAB), zinc nitrate hexahydrate ( $\text{Zn}(\text{NO}_3)_2 \cdot 6\text{H}_2\text{O}$ ), 2-methylimidazole, tetraethyl orthosilicate, sodium hydroxide (NaOH), dicyandiamide (DCM), Nafion, were purchased from aladdin. Potassium hydroxide (KOH), methanol and ethanol were obtained from Sinopharm Chemical. High purity oxygen and argon were purchased from Haipu Gas Company. All the chemicals were analytical grade and used without further purification. 18.2 MΩ cm ultrapure water purified by milli-Q instrument was used through the experiments.

### 2.2. Synthesis of CNC substrate

Firstly, 2.94 g of  $\text{Zn}(\text{NO}_3)_2 \cdot 6\text{H}_2\text{O}$  was dissolved in 100 mL of methanol, and 3.24 g of 2-methylimidazole was dissolved in another 100 mL of methanol. Then the two solutions were mixed, and stirred for 5 h at room temperature. After that, the white precipitate was centrifuged and washed with methanol for three times. The ZIF-8 was dried at 60 °C in a vacuum. Then, 600 mg of ZIF-8 was ultrasonically dispersed in 240 mL of ultrapure water, 150 mL of CTAB and 60 mg of NaOH were added, and stirred for 5 min. 1.2 mL of tetraethyl orthosilicate dispersed in 6 mL of methanol, was dropwise added to the above solution under stirring. After stirring for 0.5 h, it was centrifuged, washed, vacuum dried at 60

°C overnight. The as-obtained sample was placed in a tube furnace and pyrolyzed at 800 °C for 1 h under nitrogen flow. Then, the products were dispersed in 6 M NaOH solution, stirred at 70 °C for 12 h. Then it was centrifuged and washed with ultrapure water until neutral, and then dried in an oven at 50 °C to obtain the CNC substrate.

### 2.3. Synthesis of $\text{Ag}_1\text{Fe}_1/\text{CNC}$ , $\text{Fe}_1/\text{CNC}$ and $\text{Ag}_1/\text{CNC}$ catalyst

230 mg of CNC was dispersed in 25 mL of ultrapure water, sonicated for 1 h to make it uniformly dispersed. Then the 1 mL of  $\text{C}_2\text{AgF}_3\text{O}_2$  methanol solution ( $5 \text{ mg mL}^{-1}$ ) and 2.5 mL of  $\text{Fe}(\text{NO}_3)_3 \cdot 9\text{H}_2\text{O}$  methanol solution ( $5 \text{ mg mL}^{-1}$ ) were added dropwise, stirred for 24 h, and then lyophilized to get the precursor. The  $\text{Ag}_1\text{Fe}_1/\text{CNC}$  catalyst was obtained by calcining the precursor with 1 g of dicyandiamide at 1000 °C for 3 h under  $\text{N}_2$  atmosphere. The synthesis of  $\text{Fe}_1/\text{CNC}$  or  $\text{Ag}_1/\text{CNC}$  was carried out through similar method, except that only  $\text{C}_2\text{AgF}_3\text{O}_2$  aqueous solution or  $\text{Fe}(\text{NO}_3)_3 \cdot 9\text{H}_2\text{O}$  aqueous solution was added, respectively.

### 2.4. Characterization

The morphology of the catalysts was monitored by transmission electron microscope (TEM, FEI Tecnai G2 F20 S-Twin) with an accelerating voltage of 200 kV as well as the field-emission scanning electron microscope (FE-SEM, JEORJSM-6700F). The HAADF-STEM images were measured by JEOL JEM-ARM200F, which was worked at an accelerating voltage of 300 kV. The atomic structure of the sample was characterized by using a JEOL ARM-200CF transmission electron microscope operated at 200 kV and equipped with double spherical aberration (Cs) correctors. Powder X-ray diffraction (XRD) patterns were recorded using a Bruker AXS D8 FOCUS X-ray powder diffractometer with Cu Kα radiation. The X-ray photoelectron spectroscopy (XPS) measurements were performed with a Perkin Elmer Physics PHI 5300 spectrometer using Al Kα nonmonochromatic radiation. The metal content was measured by ICP-OES, which was carried out on Thermo Fisher IRIS Intrepid. The  $\text{N}_2$  adsorption/desorption curve was tested at 77 K using a Micromeritics ASAP 2020 surface area analyzer. Raman spectra were taken on a Renishaw inVia-Reflex spectrometer system and excited by a 514-nm laser.

### 2.5. HEMFC membrane electrode assembly tests

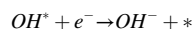
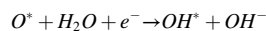
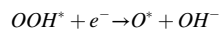
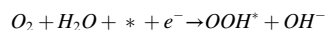
Catalyst ink was prepared by mixing catalyst with 5 wt% PAP-TP-100 ionomers (purchased from Versogen) diluted by isopropanol/water (25:1) solvent. The catalyst ink was ultrasonic treated with ice bath for 3 h and sprayed on two side of PAP-TP-85 (20 μm, purchased from Versogen) membrane with an effective area of  $5 \text{ cm}^2$  using airbrush. The commercial PtRu/C (Johnson Matthey HiSpec 10000, 40 wt% Pt and 20 wt% Ru on Vulcan XC-72) were used as anode catalyst, while the  $\text{Ag}_1\text{Fe}_1/\text{CNC}$ ,  $\text{Fe}_1/\text{CNC}$  and commercial 20 wt% Ag/C were used as cathode catalysts. The CCM and gas diffusion layer (SGL, 29BC) were assembled in a standard test cell of fixture ( $2.25 \times 2.25 \text{ cm}^2$ ). Then we tested them using Scribner 850e as condition-controlled fuel cell test station. Throughout the MEA tests, the fuel cell polarization curve was recorded at 80 °C and 100 % relative humidity. While for fuel supply and oxygen supply, the back pressures were set to 200 kPa.

### 2.6. DFT calculation

All the calculations were performed using spin-polarized density functional theory (DFT) as implemented in the Vienna Ab Initio simulation package (VASP) [55,56]. The ion-electron interaction was described using the projector augmented wave (PAW) [57]. Generalized gradient approximation (GGA) with the Perdew-Burke-Ernzerhof (PBE) functional was used to describe the exchange-correlation energy [58]. The Kohn-Sham wave functions were expanded on a plane-wave basis

with a kinetic cutoff energy of 520 eV. A  $4\sqrt{3} \times 6$  orthogonal supercell consisting of 96 carbon atoms was firstly constructed as the substrate. Fe and Ag atom were then anchored via displacing carbon atoms. The Monkhorst-Pack scheme was employed to sample the Brillouin zone using  $2 \times 3 \times 1$  k-point grid for geometry optimization and  $5 \times 7 \times 1$  k-point grid for electronic structure calculation [59]. Bader charge analysis was used to decompose the charge density into volumes around atoms [60]. In addition, the Lobster program was used to process the electronic structure information in COHP analysis. Geometry was considered optimized when the force on each atom was  $< 0.025$  eV/Å. A vacuum space  $> 15$  Å was added to all surface models to ensure no appreciable interaction between periodic images [61–63].

The theoretical overpotentials for ORR are calculated using the following mechanism:



where the \* denotes for an open surface site, the  $OH^*$ ,  $O^*$ , and  $OOH^*$  represent the adsorption intermediates in the reaction process. All adsorption energies are computed with reference to  $H_2$  and  $H_2O$ . For each individual step, the Gibbs free energy ( $\Delta G_i$ ) was calculated by using the TS and ZPE corrections in Table S5. The theoretical ORR overpotential ( $\eta_{ORR}$ ) is then defined as  $\eta_{ORR} = 1.23 \text{ V} - \min(\Delta G_1, \Delta G_2, \Delta G_3)$ ,

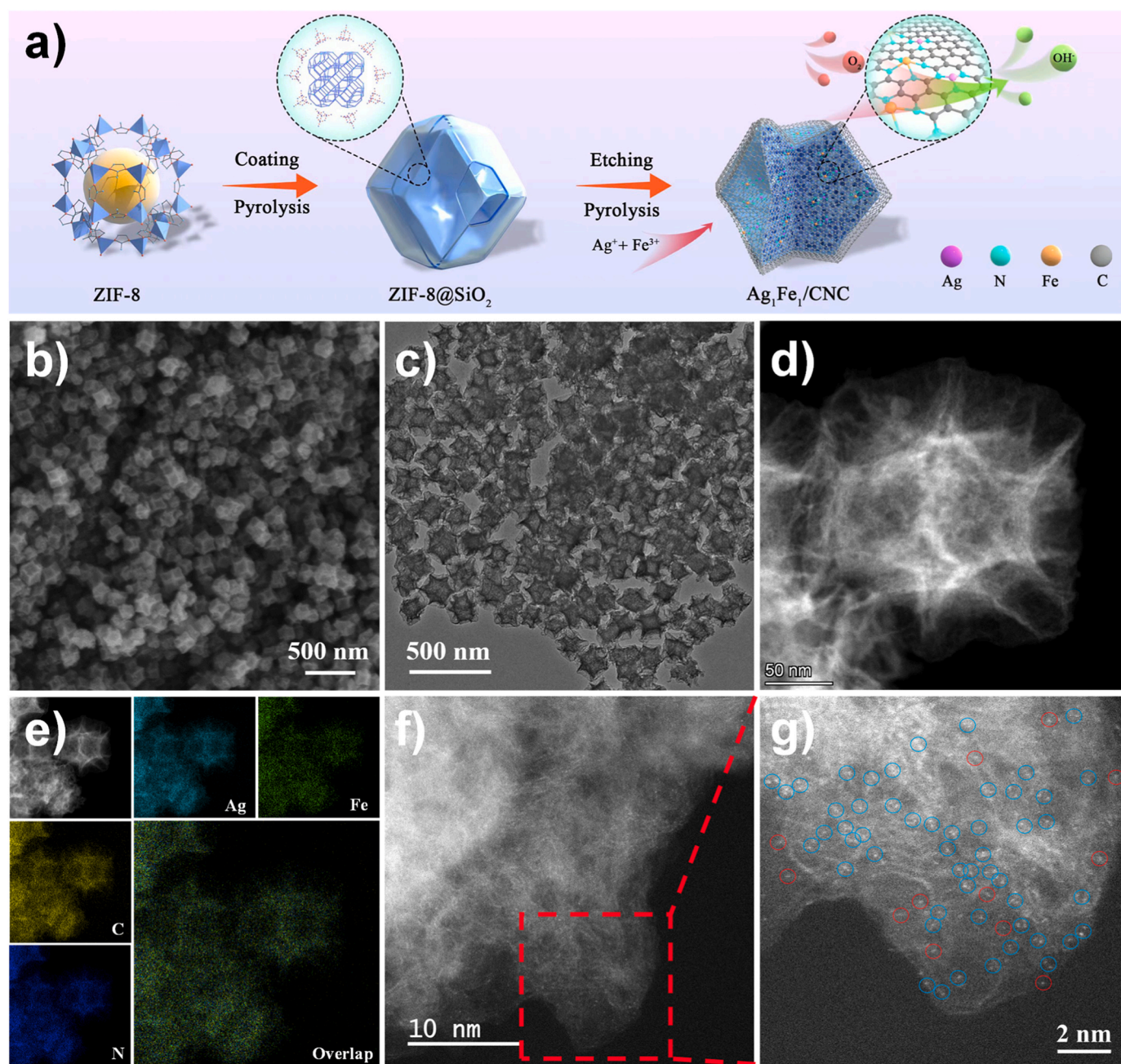


**Fig. 1.** Synthesis and electro-microscopy of the  $Ag_1Fe_1/CNC$ . (a) Schematic illustration of the synthetic approach. (b) SEM image. (c) TEM image. (d) HAADF-STEM image. (e) EDS mappings. (f) AC HAADF-STEM image. (g) Magnified AC HAADF-STEM image. The isolated single-atoms are highlighted by red circles. The blue circles highlight the adjacent single-atom sites.



$\Delta G_4)/e$ .

### 3. Results and discussion

#### 3.1. Synthesis and characterization of the $\text{Ag}_1\text{Fe}_1/\text{CNC}$

The  $\text{Ag}_1\text{Fe}_1/\text{CNC}$  was synthesized by templated controlled pyrolysis approach as illustrated in Fig. 1a. The synthesized ZIF-8 nanoparticles (transmission electron microscopy (TEM) image shown in Fig. S1a) were used as the template, and also the source for the formation of the carbon substrate. First, the prepared ZIF-8 was coated with a layer of  $\text{SiO}_2$  (TEM shown in Fig. S1b), and then it was pyrolyzed at 800 °C for 1 h to form concave N-doped carbon (CNC) substrate (TEM shown in Fig. S1c). The  $\text{SiO}_2$  layer was then removed by 6 M KOH, and Ag and Fe precursors were loaded on the CNC substrate, followed by further pyrolysis at 1000 °C for 3 h to obtain the  $\text{Ag}_1\text{Fe}_1/\text{CNC}$  catalyst.  $\text{Ag}_1/\text{CNC}$  and  $\text{Fe}_1/\text{CNC}$  were synthesized as well by similar method but only adding Ag and Fe precursor, respectively. The metal contents of the catalysts were measured by inductively coupled plasma optical emission spectrometer (ICP-OES) and summarized in Table S1. The  $\text{Ag}_1\text{Fe}_1/\text{CNC}$  had 0.58 wt% of Ag and 0.92 wt% of Fe. The  $\text{Ag}_1/\text{CNC}$  and  $\text{Fe}_1/\text{CNC}$  had the similar amount of the corresponding metals.

Fig. 1b–d show the scanning electron microscopy (SEM), transmission electron microscopy (TEM) and high-angle annular dark-field scanning transmission electron microscopy (HAADF-STEM) images of the as-obtained  $\text{Ag}_1\text{Fe}_1/\text{CNC}$ , exhibiting the concave polyhedral structure with uniform size of about 200 nm and the carbon layer thickness of about 25 nm. No clear nanoparticles or clusters were observed in the microscopy images. The EDS mappings (Fig. 1e) show the uniformly distributed Ag, Fe, N, and C in the entire polyhedron. The aberration corrected HAADF-STEM (Fig. 1f, g) images show the isolated bright spots (circled in red), indicating the atomic dispersion of Ag and Fe. Some paired spots with distance less than 0.5 nm (circled in blue in the Fig. 1f and their distances were summarized in Fig. S2) were observed, suggesting the dominated adjacent diatomic sites. Fig. S3 and S4 show the SEM, TEM, AC HAADF-STEM and EDS mapping images of  $\text{Ag}_1/\text{CNC}$  and  $\text{Fe}_1/\text{CNC}$ . They have similar concave polyhedral structures with atomically dispersed metal atoms. The X-ray diffraction (XRD, Fig. S5) patterns of catalysts only show the peaks from graphite, and no peaks related to Ag or Fe species were observed, indicating that no Ag- or Fe-based nanoparticles existed in  $\text{Ag}_1\text{Fe}_1/\text{CNC}$ ,  $\text{Ag}_1/\text{CNC}$  and  $\text{Fe}_1/\text{CNC}$  catalysts, which was consistent with the AC HAADF-STEM results.

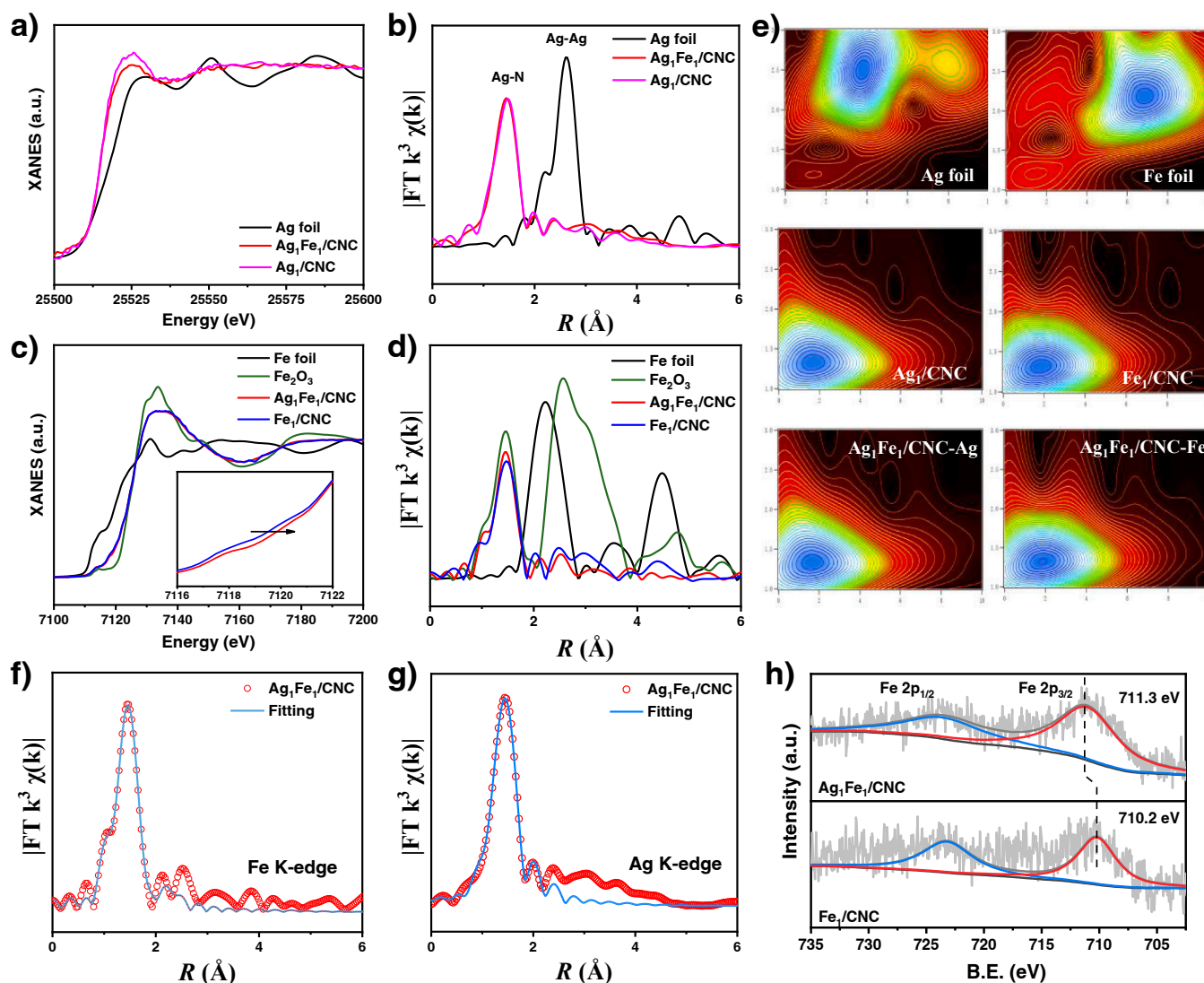


**Fig. 2.** X-ray adsorption spectroscopy of  $\text{Ag}_1\text{Fe}_1/\text{CNC}$  and the control samples. (a) Ag K-edge XANES. (b) FT-EXAFS of Ag K-edge. (c) Fe K-edge XANES. (d) FT-EXAFS of Fe K-edge. (e) WT plots of  $\text{Ag}_1\text{Fe}_1/\text{CNC}$ ,  $\text{Ag}_1/\text{CNC}$  and  $\text{Fe}_1/\text{CNC}$  in comparison with Fe foil and Ag foil. (f) Fe K-edge EXAFS spectrum fitting of  $\text{Ag}_1\text{Fe}_1/\text{CNC}$ . (g) Ag K-edge EXAFS spectrum fitting of  $\text{Ag}_1\text{Fe}_1/\text{CNC}$ . (h) The Fe 2p high resolution XPS spectra of  $\text{Ag}_1\text{Fe}_1/\text{CNC}$  and  $\text{Fe}_1/\text{CNC}$ .

### 3.2. Structural characterization of the Ag<sub>1</sub>Fe<sub>1</sub>/CNC

Fig. 2a shows the Ag K-edge X-ray absorption near-edge structure (XANES) white line spectra. Due to the special  $4d^{10}5s^1$  configuration of Ag, the white line of Ag with +1 valence shifts towards lower energy compared with the metallic Ag. It demonstrated that the Ag in Ag<sub>1</sub>Fe<sub>1</sub>/CNC and Ag<sub>1</sub>/CNC were in positive valence, and the valence state of Ag in Ag<sub>1</sub>Fe<sub>1</sub>/CNC was slightly lower than that in Ag<sub>1</sub>/CNC. Fig. 2b shows the Fourier transform  $k^3$ -weighted extended X-ray absorption fine structure (FT-EXAFS) spectra of Ag K-edge. Ag<sub>1</sub>Fe<sub>1</sub>/CNC and Ag<sub>1</sub>/CNC exhibit a peak at 1.45 Å, which was attributed to Ag–N bonding, and no Ag–Ag binding (2.62 Å) was detected, confirming that Ag species existed as single-atom form in Ag<sub>1</sub>/CNC and Ag<sub>1</sub>Fe<sub>1</sub>/CNC.

The XANES spectra for Fe K-edge of Ag<sub>1</sub>Fe<sub>1</sub>/CNC and Fe<sub>1</sub>/CNC were located between those of Fe foil and Fe<sub>2</sub>O<sub>3</sub> (Fig. 2c), proving that the valence of Fe in Ag<sub>1</sub>Fe<sub>1</sub>/CNC and Fe<sub>1</sub>/CNC was situated between 0 and +3. In addition, the Fe K-edge spectra of Ag<sub>1</sub>Fe<sub>1</sub>/CNC was more inclined to that of Fe<sub>2</sub>O<sub>3</sub> than that of Fe<sub>1</sub>/CNC, indicating the increased valence of Fe in Ag<sub>1</sub>Fe<sub>1</sub>/CNC. The FT-EXAFS spectra of Fe K-edge in Ag<sub>1</sub>Fe<sub>1</sub>/CNC and Fe<sub>1</sub>/CNC shows only a main peak at 1.47 Å attributed to Fe–N scattering, and no Fe–Fe scattering at 2.22 Å was found, proving the atomic dispersed Fe species in Fe<sub>1</sub>/CNC and Ag<sub>1</sub>Fe<sub>1</sub>/CNC (Fig. 2d). Fig. S6 was the fitting curves of the  $k$ -space and  $q$ -space EXAFS spectra.

The wavelet transform (WT) contour plots of both Ag and Fe in Ag<sub>1</sub>Fe<sub>1</sub>/CNC dual-site revealed the maximum intensity at around 1.9 Å<sup>−1</sup> (Fig. 2e), corresponding to the Ag–N and Fe–N scattering, respectively. And the corresponding Ag in Ag<sub>1</sub>/CNC and Fe in Fe<sub>1</sub>/CNC also exhibited similar location at around 1.9 Å<sup>−1</sup>. No Ag–Ag at around 3.9 Å<sup>−1</sup> or Fe–Fe at around 7.0 Å<sup>−1</sup> could be observed, substantiating that Ag and Fe species were atomically dispersed in Ag<sub>1</sub>Fe<sub>1</sub>/CNC. Moreover, the quantitative least-squares EXAFS spectra fitting to Ag<sub>1</sub>Fe<sub>1</sub>/CNC were shown in Fig. 2f and g and Table S2 and 3, illustrating the coordination number of Ag and Fe are 3 and 4, respectively. And the coordination numbers were similar to those in Ag<sub>1</sub>/CNC (2.9), and Fe<sub>1</sub>/CNC (3.9), as demonstrated in Fig. S7. In this regard, based on the XAFS and the AC HAADF-STEM results, we constructed the structure model for Ag<sub>1</sub>Fe<sub>1</sub>/CNC in the following theoretical discussion, in which Ag–N<sub>3</sub> site and Fe–N<sub>4</sub> were existed adjacently.

The chemical environment of catalysts was characterized by X-ray photoelectron spectroscopy (XPS). As shown in Fig. S8, the N 1s XPS spectrum could be deconvoluted into pyridinic N (398.6 eV), graphitic N (402.1 eV), pyrrolic N (400.9 eV) and M–N (399.6 eV) [64]. The existence of M–N peak suggested that the Fe and Ag were coordinated with N atoms. Fig. 2h shows the Fe 2p XPS spectra. The Fe 2p<sub>3/2</sub> peak in Ag<sub>1</sub>Fe<sub>1</sub>/CNC (711.3 eV) shifted to higher binding energy compared with that in Fe<sub>1</sub>/CNC (710.2 eV). The deconvolution results showed the higher Fe(III) portion in the Ag<sub>1</sub>Fe<sub>1</sub>/CNC (Fig. S9). It demonstrated that the Fe contributes partial electrons to Ag in Ag<sub>1</sub>Fe<sub>1</sub>/CNC, resulting in higher valence state of Fe. And this was consistent with the XANES results.

Fig. S10 shows the Raman spectra. The peaks at ~1350 and ~1600 cm<sup>−1</sup> were assigned to the D and G band of carbon, respectively. The I<sub>D</sub>/I<sub>G</sub> of Ag<sub>1</sub>Fe<sub>1</sub>/CNC was slightly higher than that of Ag<sub>1</sub>/CNC and Fe<sub>1</sub>/CNC, indicating that Ag<sub>1</sub>Fe<sub>1</sub>/CNC had more defects. The N<sub>2</sub> desorption isotherms and pore-sizes distributions (Fig. S11) show that Ag<sub>1</sub>Fe<sub>1</sub>/CNC had slightly larger specific surface area of 844 m<sup>2</sup> g<sup>−1</sup> than Ag<sub>1</sub>/CNC (762 m<sup>2</sup> g<sup>−1</sup>) and Fe<sub>1</sub>/CNC (736 m<sup>2</sup> g<sup>−1</sup>). It might come from the higher total metal loading of Ag<sub>1</sub>Fe<sub>1</sub>/CNC, which brought more defects. The pore sizes in Ag<sub>1</sub>Fe<sub>1</sub>/CNC were mainly distributed at ~4 nm. The above results suggested that Ag<sub>1</sub>Fe<sub>1</sub>/CNC exposed more catalytic sites, thereby increasing catalytic activity.

### 3.3. The high ORR catalytic performance of the Ag<sub>1</sub>Fe<sub>1</sub>/CNC in both RDE test and HEMFC

In order to investigate the ORR performance of the as-obtained

catalysts, we firstly performed electrochemical measurements in 0.1 M KOH electrolyte. Commercial Pt/C was tested as well as the benchmark. The cyclic voltammetry (CV) curves in Ar- and O<sub>2</sub>-saturated electrolyte are shown in Fig. S12. The reduction peak appears in O<sub>2</sub>-saturated electrolyte indicated that all the tested catalysts had oxygen reduction activity. To further quantify the ORR activity of the catalysts, electrochemical measurements based on RDE were performed, and the polarization curves obtained in O<sub>2</sub>-saturated 0.1 M KOH electrolyte are shown in Fig. 3a. The half-wave potential ( $E_{1/2}$ ) and ORR kinetic current density ( $J_k$ ) of the tested catalysts were summarized in Fig. 3b. The Ag<sub>1</sub>Fe<sub>1</sub>/CNC showed the highest ORR activity with the  $E_{1/2}$  of 0.917 V, which was higher than that for Pt/C (0.862 V), Ag<sub>1</sub>/CNC (0.884 V) and Fe<sub>1</sub>/CNC (0.870 V). The AgFe/CNC catalysts with different Ag/Fe ratios were synthesized and tested as well (Fig. S13). It was found that the optimized Ag/Fe raw material mass ratio was 1:2.5. The Ag single atom type catalysts also showed enhanced ORR activity to the Ag nanoparticle catalysts (Fig. S14). We compared the  $E_{1/2}$  of Ag<sub>1</sub>Fe<sub>1</sub>/CNC with the previously reported Ag- and Fe-based ORR catalysts in Fig. 3c and Table S4. It was found that the ORR activity of Ag<sub>1</sub>Fe<sub>1</sub>/CNC was almost the best among all the reported catalysts. The  $J_k$  for Ag<sub>1</sub>Fe<sub>1</sub>/CNC at 0.9 V was 12.96 mA cm<sup>−2</sup>, which was 9.1, 4.5, and 6.1 times higher than that of Pt/C (1.43 mA cm<sup>−2</sup>), Ag<sub>1</sub>/CNC (2.85 mA cm<sup>−2</sup>), Fe<sub>1</sub>/CNC (2.12 mA cm<sup>−2</sup>). The electrochemically active surface area (ECSA) of the single atom catalysts were estimated by the double layer capacitance ( $C_{dl}$ ), as shown in Fig. S15. The Ag<sub>1</sub>Fe<sub>1</sub>/CNC had the highest  $C_{dl}$  of 60 mF cm<sup>−2</sup>, which was 1.3 and 1.7 times as that of Ag<sub>1</sub>/CNC (47 mF cm<sup>−2</sup>) and Fe<sub>1</sub>/CNC (36 mF cm<sup>−2</sup>), respectively. The larger ECSA was beneficial for the electrocatalytic processes. However, the more significant improvement of the  $J_k$  than ECSA demonstrated that the enhanced ORR performance of Ag<sub>1</sub>Fe<sub>1</sub>/CNC was not only from the enlarged ECSA, but also improved intrinsic activities.

To quantify the intrinsic activity of each site, we calculate the turnover frequency (TOF) at 0.9 V. For the Ag<sub>1</sub>Fe<sub>1</sub>/CNC, we assumed that all the metals served as the active centers. For the Pt/C, the number of the active sites was calculated from its ECSA, which was estimated by the H<sub>upd</sub> peak in CV scans. The TOF of Pt/C at 0.9 V was 0.25 s<sup>−1</sup>, which was close to the literature data [65]. The Ag<sub>1</sub>Fe<sub>1</sub>/CNC showed a higher TOF of 0.45 s<sup>−1</sup>, illustrating the higher intrinsic ORR activity of Ag<sub>1</sub>Fe<sub>1</sub>/CNC. The Tafel slope of Ag<sub>1</sub>Fe<sub>1</sub>/CNC was evaluated as 51 mV dec<sup>−1</sup>, which was lower than that of Pt/C (Fig. S16). All the above results demonstrated the significantly enhanced ORR performance of Ag<sub>1</sub>Fe<sub>1</sub>/CNC featured by the adjunct Ag–N<sub>3</sub> and Fe–N<sub>4</sub> sites.

The H<sub>2</sub>O<sub>2</sub> yield was measured by the rotating ring disk electrode (RRDE) measurement. As shown in Fig. 3d, the HO<sub>2</sub> yield of Ag<sub>1</sub>Fe<sub>1</sub>/CNC remained below 0.5 %, confirming that Ag<sub>1</sub>Fe<sub>1</sub>/CNC catalyzed a highly efficient ORR through a four-electron pathway. The RDE measurements with different rotating speeds demonstrated similar results of the electron transfer number in range of 3.98–4.00 between 0.3 and 0.8 V through the Koutecky-Levich equation (Fig. S17). The durability of the Ag<sub>1</sub>Fe<sub>1</sub>/CNC catalyst was investigated by CV cycling between 0.7 and 1.0 V. After 5000 CV cycles, the  $E_{1/2}$  only had a small decay of 12 mV, demonstrating the good stability (Fig. 3e). The morphology characterization of Ag<sub>1</sub>Fe<sub>1</sub>/CNC after the stability test were shown in Fig. S18. It demonstrated that Ag and Fe remained atomically dispersed, indicating the good structural stability of Ag<sub>1</sub>Fe<sub>1</sub>/CNC.

The Ag<sub>1</sub>Fe<sub>1</sub>/CNC was further evaluated in the membrane electrode assembly (MEA) to study its performance in practical HEMFC applications. The MEA was fabricated by using Ag<sub>1</sub>Fe<sub>1</sub>/CNC (with the catalyst loading of 1 mg cm<sup>−2</sup>) as the cathode catalyst and PtRu/C (with the platinum group metal loading of 0.4 mg cm<sup>−2</sup>) as the anode catalyst. The MEA using Ag<sub>1</sub>/CNC, Fe<sub>1</sub>/CNC and commercial Ag/C were also studied for comparison. Compared with the MEA using Ag/C as the cathode (Fig. S19), the Ag<sub>1</sub>Fe<sub>1</sub>/CNC MEA showed higher cell voltage at 0.65 V and higher peak power density, demonstrating the high performance of the Ag<sub>1</sub>Fe<sub>1</sub>/CNC coming from its single atomic site feature. As shown in Fig. 3f, the Ag<sub>1</sub>Fe<sub>1</sub>/CNC MEA showed a high peak power

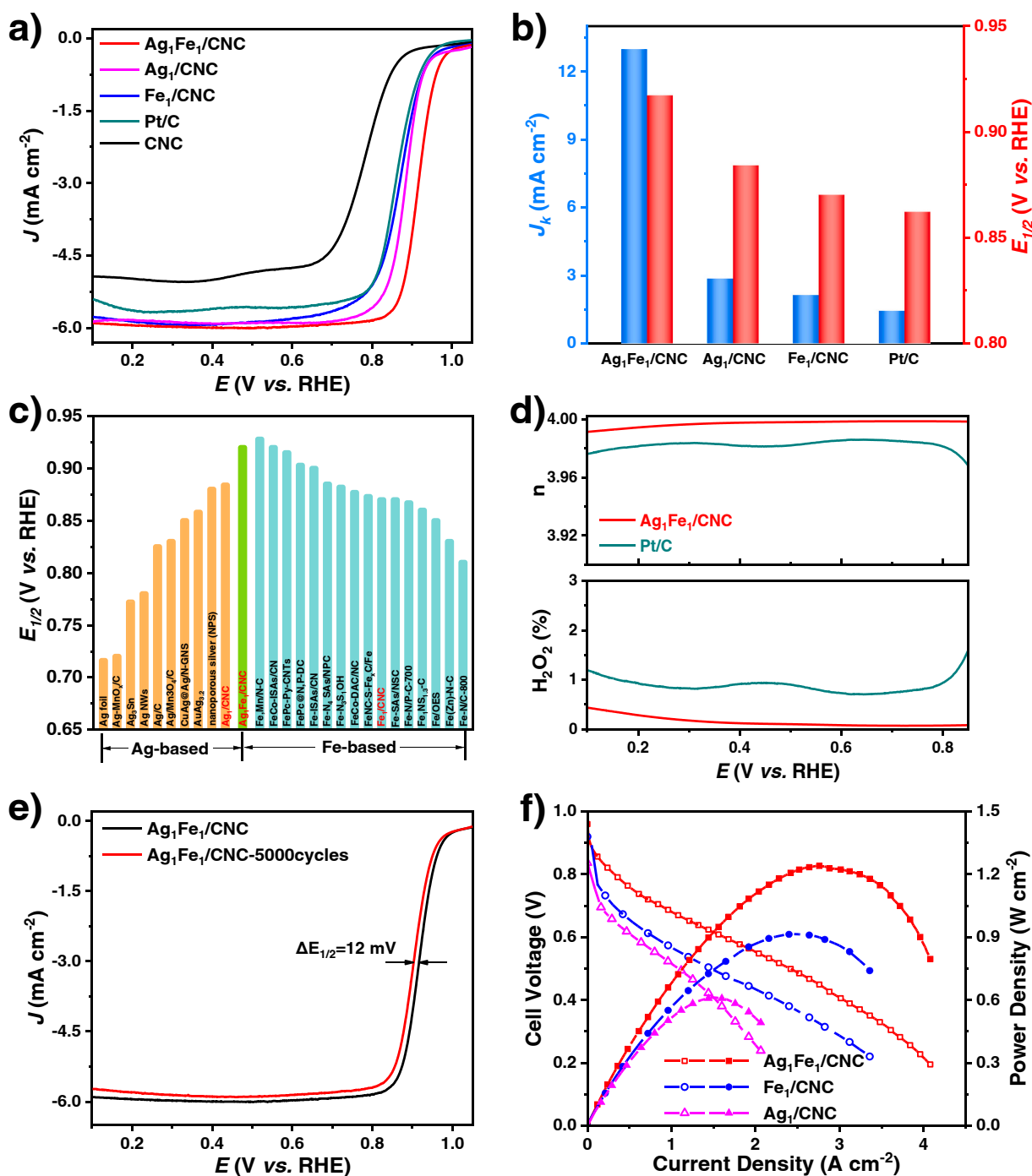


**Fig. 3.** ORR and corresponding MEA performance of Ag<sub>1</sub>Fe<sub>1</sub>/CNC. (a) ORR polarization curves obtained in O<sub>2</sub>-saturated 0.1 M KOH at 1600 rpm and scan rate of 2 mV s<sup>-2</sup>. (b) Summary of the  $J_k$  at 0.9 V and  $E_{1/2}$  for the tested catalysts. (c) Summary of the  $E_{1/2}$  of Ag<sub>1</sub>Fe<sub>1</sub>/CNC and the reported Ag- and Fe-based ORR catalysts. (d) Electron transfer numbers ( $n$ ) and HO<sub>2</sub><sup>-</sup> yield of Ag<sub>1</sub>Fe<sub>1</sub>/CNC measured by RRDE method. (e) ORR polarization curves of Ag<sub>1</sub>Fe<sub>1</sub>/CNC before and after 5000 cycles between 0.7 and 1.0 V. (f) Polarization curves and the corresponding power densities for H<sub>2</sub>-O<sub>2</sub> HEMFC (Test conditions: cell temperature at 80 °C, H<sub>2</sub> flow rate at 1.0 L min<sup>-1</sup> and O<sub>2</sub> flow rate at 1.5 L min<sup>-1</sup>, backpressures were symmetric at 200 kPa).

density of 1.26 W cm<sup>-2</sup>, which was higher than those MEAs using Ag<sub>1</sub>/CNC (0.62 W cm<sup>-2</sup>) and Fe<sub>1</sub>/CNC (0.92 W cm<sup>-2</sup>), indicating of the advantages of the Ag,Fe dual sites in HEMFC applications. The Ag<sub>1</sub>Fe<sub>1</sub>/CNC MEA also showed higher current density of 1.23 A cm<sup>-2</sup> at the cell voltage of 0.65 V, which was 3.8 and 1.9 times to those of Ag<sub>1</sub>/CNC and Fe<sub>1</sub>/CNC MEAs, respectively. The Ag<sub>1</sub>Fe<sub>1</sub>/CNC showed good durability under steady working at 0.5 A cm<sup>-2</sup>. Fig. S20 showed the chronopotentiometry curve and the voltage decreased less than 5 % after 20 h of test. The performance of the Ag<sub>1</sub>Fe<sub>1</sub>/CNC MEA surpassed

most of the reported cathode platinum-group-metal-free MEAs (Fig. S21 and Table S5). These results demonstrated that the Ag<sub>1</sub>Fe<sub>1</sub>/CNC not only had the high intrinsic ORR activity, but also had good performance in practical fuel cell applications.

#### 3.4. The significantly promoted ORR activity on the highly polarizable Ag sites

To understand the high ORR performance achieved by the Ag<sub>1</sub>Fe<sub>1</sub>/

CNC, we done the theoretical calculations through the DFT method. To have a comprehensive study, we constructed three different dual atomic Ag,Fe-N-C configurations, and set Fe and Ag coordinating with four and three N atoms (denoted as AgFe-I, AgFe-II, and AgFe-III, respectively, and the model shown in Fig. S22). The single metal structure of Ag-N<sub>3</sub> and Fe-N<sub>4</sub> are were also studied as references (model shown in Fig. S22). Bader charge analysis (results summarized in Table S6) showed that the oxidation states of Fe site in AgFe-I, AgFe-II, and AgFe-III are +1.22, +1.08, and +1.12, respectively. It demonstrated different oxidation states of Fe sites than that in the pristine Fe-N<sub>4</sub> (+1.13), indicating the electronic coupling between the Ag and Fe sites in the Ag<sub>1</sub>Fe<sub>1</sub>/CNC catalyst. The XPS and the XANES demonstrate the increased valance state of Fe in Ag<sub>1</sub>Fe<sub>1</sub>/CNC than that in Fe<sub>1</sub>/CNC, so the AgFe-I configuration was more in line with the experimental results due to its higher calculated Bader charge. Therefore, we gave priority to the AgFe-I configuration. The calculated Pourbaix diagram for Ag-N<sub>3</sub> and Fe-N<sub>4</sub> (Fig. S23) demonstrates that Fe site is covered by O\* and the Ag site with no species under ORR conditions. The same surface resting states were considered for studying the ORR free energy profile on the AgFe system.

The association mechanism was generally applied to the ORR process of the single atom catalysts [66,67]. Specifically, the ORR process underwent four proton coupled electron transfer steps, and the \*OOH, \*O and \*OH are the adsorbed intermediates. A typical ORR process on the

Ag site of AgFe-I configuration was illustrated in Fig. 4a. The free energy diagram was calculated, and the detailed calculated configuration for each site was summarized in Fig. S24–28. The calculated energy barriers for each step at the equilibrium potential were summarized in Table S7. Fig. 4b shows the free energy diagram for AgFe-I, Ag-N<sub>3</sub> and Fe-N<sub>4</sub> sites, and the rate determine steps (RDS) for each site were marked. For the Fe-N<sub>4</sub> sites, owing to the high oxyphilic of the Fe, it showed strong adsorption to the oxygen species, and the desorption of the \*OH was the rate determine step with the energy barrier of 0.766 V. For Ag-N<sub>3</sub> sites, because of the inert nature of Ag, it showed weak adsorption to the oxygen species, and the formation of \*O is identified as the rate determine step with the energy barrier of 0.601 V. The adsorption energies were optimized in the AgFe-I. For the Ag site in AgFe-I, due to the coupling between Ag and Fe, the adsorption of the oxygen species was strengthened, and the energy barriers for the formation of \*OOH and \*O was lowered. It demonstrated that Ag site in AgFe-I was highly active for ORR with a low overpotential of only 0.398 V. Compared with the Ag-N<sub>3</sub> sites, the energy barrier on Ag site in AgFe-I reduced 0.203 V, which demonstrated the significantly increased ORR activity. For the Fe site in AgFe-I, the calculated overpotential was 0.664 V, reduced 0.102 V compared with that for Fe-N<sub>4</sub> sites. It suggested that the Ag site in AgFe-I was remarkably tuned by the adjunct Fe sites, and served as the active sites for ORR. And the energy tuned level on Ag site was much

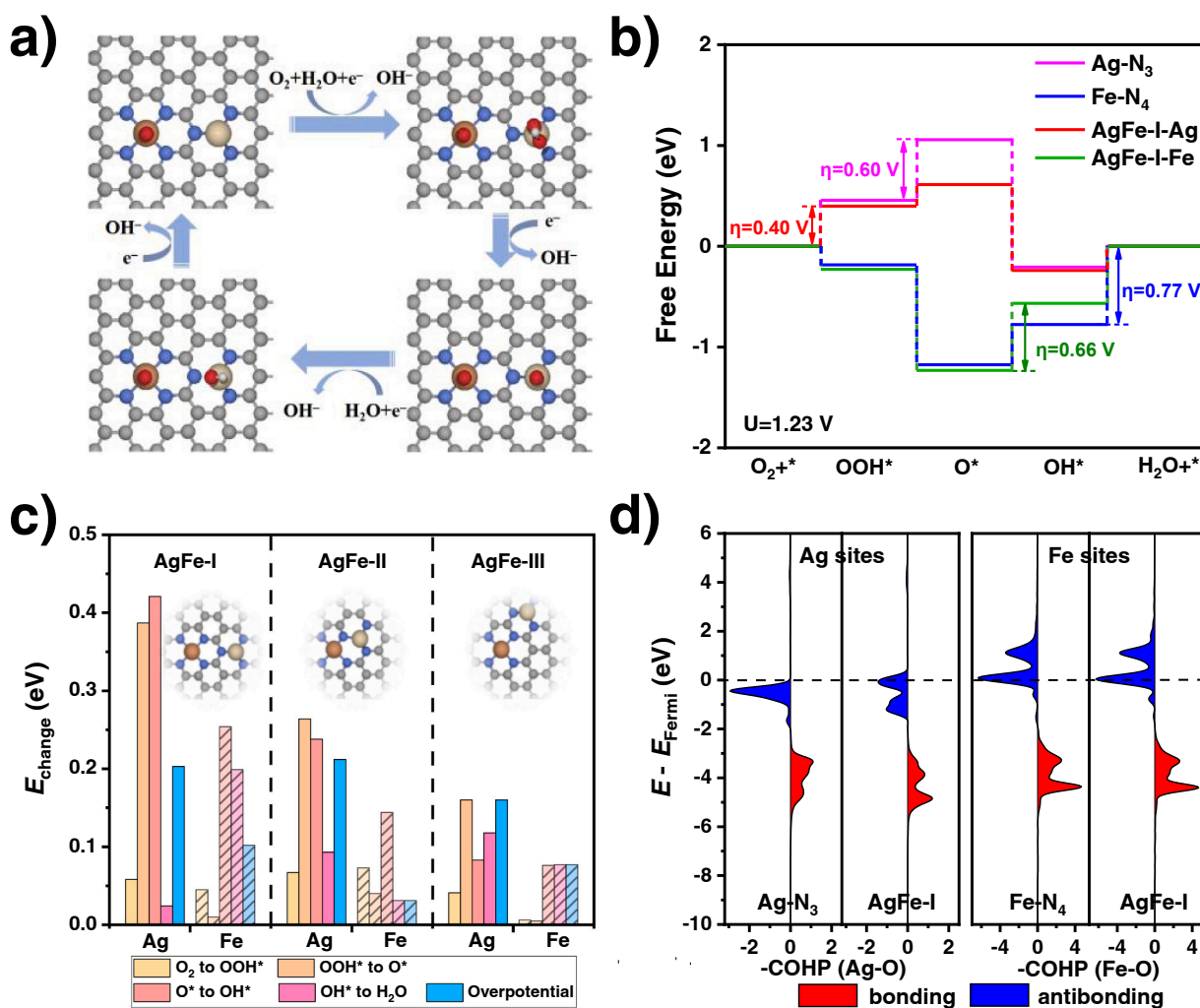


**Fig. 4.** DFT calculation results. (a) The schematic illustration of the ORR pathway on the Ag site of AgFe-I. N in red, C in gray, N in blue, Ag in silver, Fe in brown, O in red and H in white. (b) The free energy diagrams of Fe-N<sub>4</sub>, Ag-N<sub>3</sub>, Fe and Ag sites of AgFe-I. The labeled potential is for the rate determine step. (c) Free energy changes of each ORR step and overpotential (inset: the three structural models of AgFe-I, AgFe-II and AgFe-III). (d) COHP analysis of Ag and Fe sites 4d/3d and O 2p orbitals. The red and blue area represents the bonding and antibonding component, respectively.



larger than it on Fe site. Similar results were found for AgFe-II and AgFe-III configurations as well.

To illustrate the tunability of the sites, we studied the changes of the energy barrier ( $E_{\text{change}}$ ), which was defined as differences of the energy barrier of the reaction step or RDS between the site tuned by the adjunct metal atoms (e.g., Ag site in AgFe-I configuration) and the pristine metal site (e.g., Ag site in Ag-N<sub>3</sub> configuration). Clearly, a larger of  $E_{\text{change}}$  means the sites was more tunable. Fig. 4c summarized the calculated  $E_{\text{change}}$  of Ag and Fe sites with various configurations. It was found that for all of the Ag sites in AgFe-I, AgFe-II and AgFe-III, the binding energies of the intermediates were apart from those for Ag-N<sub>3</sub> site, demonstrating by the larger  $E_{\text{change}}$  compared with those on Fe sites. It illustrated the high tuning ability of the Ag sites. The more tunable Ag sites were attributed to their low valence states, which brought high polarizability. Due to the highly polarizable Ag sites, the overpotential lowered from 0.6 V for Ag-N<sub>3</sub> to 0.4 V on all of the Ag sites in AgFe-I, AgFe-II and AgFe-III, with the reduction of about 0.2 V, making them more suitable for ORR.

With the high polarizability of the Ag sites, the Ag-O interaction was enhanced in the AgFe configuration. To understand the chemical-bonding nature of enhanced Ag-O interaction in AgFe-I and the corresponding electronic-structure foundation, crystal orbital Hamiltonian population (COHP) analysis was performed. Fig. 4d compared the COHP curves between Ag 4d and O 2p orbitals of Ag-N<sub>3</sub> and AgFe-I. The blue and red filled curve represented the anti-bonding and bonding components, respectively. Due to the highly polarizable Ag sites, the orbital profile changed intensively when forming the AgFe-I. The anti-bonding states in the AgFe-I shift up with respect to that of Ag-N<sub>3</sub>, leading to a substantially lowered occupation of the Ag-O anti-bonding states and consequently stronger Ag-O interaction. Moreover, the stronger Ag-O interaction in AgFe-I was also consistent with the calculated net bonding capabilities as expressed by the integrated COHP (ICOHP). The ICOHP value of Ag in AgFe-I increased from 0.12 (Ag-N<sub>3</sub>) to 0.34. The increased Ag-O interaction lowers the energy barrier for the O adsorption, thus the ORR activity increases on the AgFe-I.

We also calculate the COHP for the Fe sites in Fe-N<sub>4</sub> and AgFe-I configurations (Fig. 4d). More anti-bonding states were unoccupied, thus the Fe-O interaction was stronger than the Ag-O interaction, and this consisted with calculated free energy diagram showing the desorption of the intermediates as the RDS. However, the COHP of the Fe in AgFe-I did not change too much compared with the Fe-N<sub>4</sub>. The ICOHP value of Fe in AgFe-I was 4.37, while it was 4.31 in Fe-N<sub>4</sub>. It further confirmed that with the improved polarizability, the Ag site was easily tuned by the coordination environment, and thus improved ORR activity was achieved.

The addition of Ag may also change the fine structure of Fe sites. The recent report demonstrated that the addition Co or Sn to the Fe-N-C materials enhanced the relative abundance of high-spin Fe(III)-N<sub>4</sub> sites, and thus improved their ORR performance in acid [68]. From the XANES results, the Fe in Ag<sub>1</sub>Fe<sub>1</sub>/CNC had slightly higher valence state than the Fe in Fe<sub>1</sub>/CNC. This might contributed to the high ORR performance of Ag<sub>1</sub>Fe<sub>1</sub>/CNC as well.

#### 4. Conclusions

In conclusion, a dual metal catalyst Ag<sub>1</sub>Fe<sub>1</sub>/CNC, with the Ag, Fe single atomic sites embedded in concave nitrogen doped carbon, has been successfully synthesized and shown high activity towards ORR. It shows a high ORR  $E_{1/2}$  of 0.917 V in RDE test, and a high peak power density of 1.26 W cm<sup>-2</sup> when it used as cathode catalyst for HEMFC. The DFT calculation demonstrates that the electronic properties of the Ag site are significantly tuned by the adjacent Fe sites, and it has a low theoretical ORR overpotential of about 0.4 V. It is found the Ag site with high polarizability is more tunable than the Fe site, which leading to the Ag site with high ORR activity. These results demonstrated that the highly polarizable metal sites are easily to be tuned by the coordination

environment towards higher catalytic performance, which may broad the route for catalyst design.

#### CRediT authorship contribution statement

**Rui Sui:** Investigation, Methodology, Electrochemical performance tests, Data analysis, Writing – original draft. **Jing Chai:** DFT calculation. **Xuerui Liu:** HEMFC membrane electrode assembly tests. **Jiajing Pei:** Physicochemical characterization, Investigation. **Xuejiang Zhang:** Physicochemical characterization. **Xingdong Wang:** Physicochemical characterization. **Yu Wang:** XAFS characterizations and data analysis. **Juncai Dong:** the WT test. **Wei Zhu:** Conceptualization, Formal analysis. **Wenxing Chen:** XAFS characterizations and data analysis. **Liang Zhang:** DFT calculation. **Zhongbin Zhuang:** Conceptualization, Methodology, Supervision, Writing – review & editing, Resources.

#### Declaration of Competing Interest

The authors declare that they have no known competing financial interests or personal relationships that could have appeared to influence the work reported in this paper.

#### Data Availability

Data will be made available on request.

#### Acknowledgements

This work was supported by the National Key Research and Development Program of China (2019YFA0210300), National Natural Science Foundation of China (21971008, 22101016, 22103047), Beijing Natural Science Foundation (Z210016), and Fundamental Research Funds for the Central Universities (buctrc201916, buctrc201823). The authors thank the BL1W1B in the Beijing Synchrotron Radiation Facility (BSRF), BL14W1 in the Shanghai Synchrotron Radiation Facility (SSRF) for help with characterizations.

#### Supporting Information

Detailed experimental characterizations, XAFS measurements, DFT calculation, and figures (SEM, TEM, XRD, Raman, BET, etc.). Table S1 shows ICP results of the prepared catalysts. Table S2 and S3 shows the structural parameters extracted from the Fe and Ag K-edge EXAFS fitting. Table S4 shows the summary of the ORR activities of reported catalysts in 0.1 M KOH. Table S5 shows summary of HEMFCs performances using platinum-group-metal free cathode. Table S6 shows the calculated Bader charge. Table S7 shows the Gibbs free energy of different intermediates.

#### Appendix A. Supporting information

Supplementary data associated with this article can be found in the online version at doi:10.1016/j.apcatb.2023.123251.

#### References

- [1] Z.P. Cano, D. Banham, S. Ye, A. Hintennach, J. Lu, M. Fowler, Z. Chen, Batteries and fuel cells for emerging electric vehicle markets, *Nat. Energy* 3 (2018) 279–289.
- [2] H.A. Gasteiger, N.M. Markovic, Just a dream—or future reality? *Science* 324 (2009) 48–49.
- [3] M.K. Debe, Electrocatalyst approaches and challenges for automotive fuel cells, *Nature* 486 (2012) 43–51.
- [4] S. Sui, X. Wang, X. Zhou, Y. Su, S. Riffat, C.-j. Liu, A comprehensive review of Pt electrocatalysts for the oxygen reduction reaction: nanostructure, activity, mechanism and carbon support in pem fuel cells, *J. Mater. Chem. A* 5 (2017) 1808–1825.
- [5] A. Kongkanand, M.F. Mathias, The priority and challenge of high-power performance of low-platinum proton-exchange membrane fuel cells, *J. Phys. Condens. Matter* 7 (2016) 1127–1137.



- [6] B.P. Setzler, Z. Zhuang, J.A. Wittkopf, Y. Yan, Activity targets for nanostructured platinum-group-metal-free catalysts in hydroxide exchange membrane fuel cells, *Nat. Nanotechnol.* 11 (2016) 1020–1025.
- [7] J.R. Varcoe, P. Atanassov, D.R. Dekel, A.M. Herring, M.A. Hickner, P.A. Kohl, A. R. Kucernak, W.E. Mustain, K. Nijmeijer, K. Scott, T. Xu, L. Zhuang, Anion-exchange membranes in electrochemical energy systems, *Energy Environ. Sci.* 7 (2014) 3135–3191.
- [8] D.R. Dekel, Review of cell performance in anion exchange membrane fuel cells, *J. Power Sources* 375 (2018) 158–169.
- [9] X. Peng, T.J. Omasta, E. Magliocca, L. Wang, J.R. Varcoe, W.E. Mustain, Nitrogen-doped carbon-CoO<sub>x</sub> nanohybrids: a precious metal free cathode that exceeds 1.0 W cm<sup>-2</sup> peak power and 100 h life in anion-exchange membrane fuel cells, *Angew. Chem. Int. Ed.* 58 (2019) 1046–1051.
- [10] Y. Xue, X. Wang, X. Zhang, J. Fang, Z. Xu, Y. Zhang, X. Liu, M. Liu, W. Zhu, Z. Zhuang, Cost-effective hydrogen oxidation reaction catalysts for hydroxide exchange membrane fuel cells, *Acta Phys.-Chim. Sin.* 37 (2020), 2009103.
- [11] H. Ren, Y. Wang, Y. Yang, X. Tang, Y. Peng, H. Peng, L. Xiao, J. Lu, H.D. Abruna, L. Zhuang, Fe/N/C nanotubes with atomic Fe sites: a highly active cathode catalyst for alkaline polymer electrolyte fuel cells, *ACS Catal.* 7 (2017) 6485–6492.
- [12] S. Huang, Z. Qiao, P. Sun, K. Qiao, K. Pei, L. Yang, H. Xu, S. Wang, Y. Huang, Y. Yan, D. Cao, The strain induced synergistic catalysis of FeN<sub>4</sub> and MnN<sub>3</sub> dual-site catalysts for oxygen reduction in proton-/anion-exchange membrane fuel cells, *Appl. Catal. B* 317 (2022), 121770.
- [13] J.-C. Li, S. Maurya, Y.S. Kim, T. Li, L. Wang, Q. Shi, D. Liu, S. Feng, Y. Lin, M. Shao, Stabilizing single-atom iron electrocatalysts for oxygen reduction via ceria confining and trapping, *ACS Catal.* 10 (2020) 2452–2458.
- [14] J. Lilloja, E. Kibena-Poldsepp, A. Sarapu, M. Kodali, Y. Chen, T. Asset, M. Käärik, M. Merisalu, P. Paiste, J. Aruväli, A. Treshchalov, M. Rähn, J. Leis, V. Sammelselg, S. Holdcroft, P. Atanassov, K. Tammeveski, Cathode catalysts based on cobalt- and nitrogen-doped nanocarbon composites for anion exchange membrane fuel cells, *ACS Appl. Energy Mater.* 3 (2020) 5375–5384.
- [15] H. Adabi, A. Shakouri, N. Ul Hassan, J.R. Varcoe, B. Zulevi, A. Serov, J. R. Regalado, W.E. Mustain, High-performing commercial Fe–N–C cathode electrocatalyst for anion-exchange membrane fuel cells, *Nat. Energy* 6 (2021) 834–843.
- [16] J. Yang, W. Liu, M. Xu, X. Liu, H. Qi, L. Zhang, X. Yang, S. Niu, D. Zhou, Y. Liu, Y. Su, J.F. Li, Z.Q. Tian, W. Zhou, A. Wang, T. Zhang, Dynamic behavior of single-atom catalysts in electrocatalysis: identification of Cu–N<sub>3</sub> as an active site for the oxygen reduction reaction, *J. Am. Chem. Soc.* 143 (2021) 14530–14539.
- [17] L. Li, S. Huang, R. Cao, K. Yuan, C. Lu, B. Huang, X. Tang, T. Hu, X. Zhuang, Y. Chen, Optimizing microenvironment of asymmetric N,S-coordinated single-atom Fe via axial fifth coordination toward efficient oxygen electroreduction, *Small* 18 (2022), e2105387.
- [18] C.X. Zhao, B.Q. Li, J.N. Liu, Q. Zhang, Intrinsic electrocatalytic activity regulation of M–N–C single-atom catalysts for the oxygen reduction reaction, *Angew. Chem. Int. Ed.* 60 (2021) 4448–4463.
- [19] C. Zhu, S. Fu, Q. Shi, D. Du, Y. Lin, Single-atom electrocatalysts, *Angew. Chem. Int. Ed.* 56 (2017) 13944–13960.
- [20] A. Schoedel, M. Li, D. Li, M. O’Keeffe, O.M. Yaghi, Structures of metal-organic frameworks with rod secondary building units, *Chem. Rev.* 116 (2016) 12466–12535.
- [21] M.M. Hossen, K. Artyushkova, P. Atanassov, A. Serov, Synthesis and characterization of high performing Fe–N–C catalyst for oxygen reduction reaction (ORR) in alkaline exchange membrane fuel cells, *J. Power Sources* 375 (2018) 214–221.
- [22] K. Im, D. Kim, J.-H. Jang, J. Kim, S.J. Yoo, Hollow-sphere Co–NC synthesis by incorporation of ultrasonic spray pyrolysis and pseudomorphic replication and its enhanced activity toward oxygen reduction reaction, *Appl. Catal. B* 260 (2020), 118192.
- [23] X. Cui, W. Li, P. Ryabchuk, K. Junge, M. Beller, Bridging homogeneous and heterogeneous catalysis by heterogeneous single-metal-site catalysts, *Nat. Catal.* 1 (2018) 385–397.
- [24] Y. Wang, H. Su, Y. He, L. Li, S. Zhu, H. Shen, P. Xie, X. Fu, G. Zhou, C. Feng, D. Zhao, F. Xiao, X. Zhu, Y. Zeng, M. Shao, S. Chen, G. Wu, J. Zeng, C. Wang, Advanced electrocatalysts with single-metal-atom active sites, *Chem. Rev.* 120 (2020) 12217–12314.
- [25] H.T. Chung, D.A. Cullen, D. Higgins, B.T. Sneed, E.F. Holby, K.L. More, P. Zelenay, Direct atomic-level insight into the active sites of a high-performance PGM-free ORR catalyst, *Science* 357 (2017) 479–484.
- [26] Y. Yang, X. Xu, P. Sun, H. Xu, L. Yang, X. Zeng, Y. Huang, S. Wang, D. Cao, Ag<sub>NPs</sub>@ Fe–N–C oxygen reduction catalysts for anion exchange membrane fuel cells, *Nano Energy* 100 (2022), 107466.
- [27] G. Yang, J. Zhu, P. Yuan, Y. Hu, G. Qu, B.A. Lu, X. Xue, H. Yin, W. Cheng, J. Cheng, W. Xu, J. Li, J. Hu, S. Mu, J.N. Zhang, Regulating Fe-spin state by atomically dispersed Mn–N in Fe–N–C catalysts with high oxygen reduction activity, *Nat. Commun.* 12 (2021) 1734.
- [28] S. Liu, Z. Li, C. Wang, W. Tao, M. Huang, M. Zuo, Y. Yang, K. Yang, L. Zhang, S. Chen, P. Xu, Q. Chen, Turning main-group element magnesium into a highly active electrocatalyst for oxygen reduction reaction, *Nat. Commun.* 11 (2020) 938.
- [29] J.K. Nørskov, J. Rossmeisl, A. Logadottir, L. Lindqvist, Origin of the overpotential for oxygen reduction at a fuel-cell cathode, *J. Phys. Chem. B* 108 (2004) 17886–17892.
- [30] A.E. Russell, Electrocatalysis: theory and experiment at the interface, *Phys. Chem. Chem. Phys.* 10 (2008) 3607–3608.
- [31] X. Li, H. Rong, J. Zhang, D. Wang, Y. Li, Modulating the local coordination environment of single-atom catalysts for enhanced catalytic performance, *Nano Res.* 13 (2020) 1842–1855.
- [32] S. Tian, M. Hu, Q. Xu, W. Gong, W. Chen, J. Yang, Y. Zhu, C. Chen, J. He, Q. Liu, H. Zhao, D. Wang, Y. Li, Single-atom Fe with Fe<sub>1</sub>N<sub>3</sub> structure showing superior performances for both hydrogenation and transfer hydrogenation of nitrobenzene, *Sci. China Mater.* 64 (2020) 642–650.
- [33] H. Jin, J. Zhu, R. Yu, W. Li, P. Ji, L. Liang, B. Liu, C. Hu, D. He, S. Mu, Tuning the Fe–N<sub>4</sub> sites by introducing Bi–O bonds in a Fe–N–C system for promoting the oxygen reduction reaction, *J. Mater. Chem. A* 10 (2022) 664–671.
- [34] V. Stamenkovic, B.S. Mun, K.J. Mayrhofer, P.N. Ross, N.M. Markovic, J. Rossmeisl, J. Greeley, J.K. Nørskov, Changing the activity of electrocatalysts for oxygen reduction by tuning the surface electronic structure, *Angew. Chem. Int. Ed.* 45 (2006) 2897–2901.
- [35] L. Hu, C. Dai, L. Chen, Y. Zhu, Y. Hao, Q. Zhang, L. Gu, X. Feng, S. Yuan, L. Wang, B. Wang, Metal-triazolate-framework-derived FeN<sub>4</sub>Cl<sub>1</sub> single-atom catalysts with hierarchical porosity for the oxygen reduction reaction, *Angew. Chem. Int. Ed.* 60 (2021) 27324–27329.
- [36] X. Zheng, J. Wu, X. Cao, J. Abbott, C. Jin, H. Wang, P. Strasser, R. Yang, X. Chen, G. Wu, N-, P-, and S-doped graphene-like carbon catalysts derived from onium salts with enhanced oxygen chemisorption for Zn-air battery cathodes, *Appl. Catal. B* 241 (2019) 442–451.
- [37] Y. Chen, R. Gao, S. Ji, H. Li, K. Tang, P. Jiang, H. Hu, Z. Zhang, H. Hao, Q. Qu, X. Liang, W. Chen, J. Dong, D. Wang, Y. Li, Atomic-level modulation of electronic density at cobalt single-atom sites derived from metal-organic frameworks: enhanced oxygen reduction performance, *Angew. Chem. Int. Ed.* 60 (2021) 3212–3221.
- [38] H. Shang, X. Zhou, J. Dong, A. Li, X. Zhao, Q. Liu, Y. Lin, J. Pei, Z. Li, Z. Jiang, D. Zhou, L. Zheng, Y. Wang, J. Zhou, Z. Yang, R. Cao, R. Sarangi, T. Sun, X. Yang, X. Zheng, W. Yan, Z. Zhuang, J. Li, W. Chen, D. Wang, J. Zhang, Y. Li, Engineering unsymmetrically coordinated Cu–S<sub>2</sub>N<sub>3</sub> single atom sites with enhanced oxygen reduction activity, *Nat. Commun.* 11 (2020) 3049.
- [39] R. Sui, X. Zhang, X. Wang, X. Wang, J. Pei, Y. Zhang, X. Liu, W. Chen, W. Zhu, Z. Zhuang, Silver based single atom catalyst with heteroatom coordination environment as high performance oxygen reduction reaction catalyst, *Nano Res.* 15 (2022) 7968–7975.
- [40] Q.K. Li, X.F. Li, G. Zhang, J. Jiang, Cooperative spin transition of monodispersed FeN<sub>3</sub> sites within graphene induced by CO adsorption, *J. Am. Chem. Soc.* 140 (2018) 15149–15152.
- [41] D. Zhang, W. Chen, Z. Li, Y. Chen, L. Zheng, Y. Gong, Q. Li, R. Shen, Y. Han, W. C. Cheong, L. Gu, Y. Li, Isolated Fe and Co dual active sites on nitrogen-doped carbon for a highly efficient oxygen reduction reaction, *Chem. Commun.* 54 (2018) 4274–4277.
- [42] M. Liu, N. Li, S. Cao, X. Wang, X. Lu, L. Kong, Y. Xu, X.H. Bu, A "pre-constrained metal twins" strategy to prepare efficient dual-metal-atom catalysts for cooperative oxygen electrocatalysis, *Adv. Mater.* 34 (2022), 2107421.
- [43] D. Liu, B. Wang, H. Li, S. Huang, M. Liu, J. Wang, Q. Wang, J. Zhang, Y. Zhao, Distinguished Zn,Co–N<sub>x</sub>–C–S<sub>y</sub> active sites confined in dendritic carbon for highly efficient oxygen reduction reaction and flexible Zn-air batteries, *Nano Energy* 58 (2019) 277–283.
- [44] V. Dimitrov, T. Komatsu, Correlation among electronegativity, cation polarizability, optical basicity and single bond strength of simple oxides, *J. Solid State Chem.* 196 (2012) 574–578.
- [45] J.J. Molina, S. Lectez, S. Tazi, M. Salanne, J.F. Dufreche, J. Roques, E. Simoni, P. A. Madden, P. Turq, Ions in solutions: determining their polarizabilities from first-principles, *J. Chem. Phys.* 134 (2011), 014511.
- [46] F. Chen, H. Huang, L. Guo, Y. Zhang, T. Ma, The role of polarization in photocatalysis, *Angew. Chem. Int. Ed.* 58 (2019) 10061–10073.
- [47] Y. Zhou, A.J. Martín, F. Dattila, S. Xi, N. López, J. Pérez-Ramírez, B.S. Yeo, Long-chain hydrocarbons by CO<sub>2</sub> electroreduction using polarized nickel catalysts, *Nat. Catal.* 5 (2022) 545–554.
- [48] P. Yin, T. Yao, Y. Wu, L. Zheng, Y. Lin, W. Liu, H. Ju, J. Zhu, X. Hong, Z. Deng, G. Zhou, S. Wei, Y. Li, Single cobalt atoms with precise N-coordination as superior oxygen reduction reaction catalysts, *Angew. Chem. Int. Ed.* 55 (2016) 10800–10805.
- [49] H. Shang, W. Sun, R. Sui, J. Pei, L. Zheng, J. Dong, Z. Jiang, D. Zhou, Z. Zhuang, W. Chen, J. Zhang, D. Wang, Y. Li, Engineering isolated Mn–N<sub>2</sub>C<sub>2</sub> atomic interface sites for efficient bifunctional oxygen reduction and evolution reaction, *Nano Lett.* 20 (2020) 5443–5450.
- [50] L. Jiao, R. Zhang, G. Wan, W. Yang, X. Wan, H. Zhou, J. Shui, S.H. Yu, H.L. Jiang, Nanocasting SiO<sub>2</sub> into metal-organic frameworks imparts dual protection to high-loading Fe single-atom electrocatalysts, *Nat. Commun.* 11 (2020) 2831.
- [51] S. Gu, W. Sheng, R. Cai, S.M. Alia, S. Song, K.O. Jensen, Y. Yan, An efficient Ag-ionomer interface for hydroxide exchange membrane fuel cells, *Chem. Commun.* 49 (2013) 131–133.
- [52] L. Wang, X. Peng, W.E. Mustain, J.R. Varcoe, Radiation-grafted anion-exchange membranes: the switch from low- to high-density polyethylene leads to remarkably enhanced fuel cell performance, *Energy Environ. Sci.* 12 (2019) 1575–1579.
- [53] S. Lu, J. Pan, A. Huang, L. Zhuang, J. Lu, Alkaline polymer electrolyte fuel cells completely free from noble metal catalysts, *PANS* 105 (2008) 20611–20614.
- [54] J. Wang, Y. Zhao, B.P. Setzler, S. Rojas-Carbonell, C. Ben Yehuda, A. Amel, M. Page, L. Wang, K. Hu, L. Shi, S. Gottesfeld, B. Xu, Y. Yan, Poly(aryl piperidinium) membranes and ionomers for hydroxide exchange membrane fuel cells, *Nat. Energy* 4 (2019) 392–398.

- [55] G. Kresse, J. Furthmüller, Efficiency of ab-initio total energy calculations for metals and semiconductors using a plane-wave basis set, *Comput. Mater. Sci.* 6 (1996) 15–50.
- [56] G. Kresse, J. Hafner, Ab initio molecular dynamics for liquid metals, *Phys. Rev. B Condens Matter* 47 (1993) 558–561.
- [57] G. Kresse, D. Joubert, From ultrasoft pseudopotentials to the projector augmented-wave method, *Phys. Rev. B* 59 (1999) 1758–1775.
- [58] J.P. Perdew, K. Burke, M. Ernzerhof, Generalized gradient approximation made simple, *Phys. Rev. Lett.* 77 (1996) 3865–3868.
- [59] D.J. Chadi, Special points for Brillouin-zone integrations, *Phys. Rev. B* 16 (1977) 1746–1747.
- [60] W. Tang, E. Sanville, G. Henkelman, A. Grid-Based, Bader analysis algorithm without lattice bias, *J. Phys. Condens. Matter* 21 (2009), 084204.
- [61] S. Maintz, V.L. Deringer, A.L. Tchougreeff, R. Dronskowski, Analytic projection from plane-wave and PAW wavefunctions and application to chemical-bonding analysis in solids, *J. Comput. Chem.* 34 (2013) 2557–2567.
- [62] R. Nelson, C. Ertural, J. George, V.L. Deringer, G. Hautier, R. Dronskowski, LOBSTER: local orbital projections, atomic charges, and chemical-bonding analysis from projector-augmented-wave-based density-functional theory, *J. Comput. Chem.* 41 (2020) 1931–1940.
- [63] R. Dronskowski, P.E. Bloechl, Crystal orbital Hamilton populations (COHP): energy-resolved visualization of chemical bonding in solids based on density-functional calculations, *J. Phys. Chem.* 97 (2002) 8617–8624.
- [64] U. Tylus, Q. Jia, K. Strickland, N. Ramaswamy, A. Serov, P. Atanassov, S. Mukerjee, Elucidating oxygen reduction active sites in pyrolyzed metal-nitrogen coordinated non-precious-metal electrocatalyst systems, *J. Phys. Chem. C* 118 (2014) 8999–9008.
- [65] U.A. Paulus, A. Wokaun, G.G. Scherer, T.J. Schmidt, V. Stamenkovic, N. Markovic, P.N. Ross, Oxygen reduction on high surface area Pt-based alloy catalysts in comparison to well defined smooth bulk alloy electrodes, *Electrochim. Acta* 47 (2002) 3787–3798.
- [66] A. Kulkarni, S. Siahrostami, A. Patel, J.K. Nørskov, Understanding catalytic activity trends in the oxygen reduction reaction, *Chem. Rev.* 118 (2018) 2302–2312.
- [67] J.K. Nørskov, J. Rossmeisl, A. Logadottir, L. Lindqvist, Origin of the overpotential for oxygen reduction at a fuel-cell cathode, *J. Phys. Chem. B* 108 (2004) 17886–17892.
- [68] F. Luo, A. Roy, M.T. Sougrati, A. Khan, D.A. Cullen, X. Wang, M. Primbs, A. Zitolo, F. Jaouen, P. Strasser, Structural and reactivity effects of secondary metal doping into iron-nitrogen-carbon catalysts for oxygen electroreduction, *J. Am. Chem. Soc.* 145 (2023) 14737–14747.